Study on Corrosion Resistance of Alkali-Heat Modified Magnesium Alloy Surface

Jiyuan Zhu[1] · Chenxi Jia[1] · Yuanzhen Duan[1]

Abstract

Nowadays, it is still challenging to simply and efficiently prepare corrosion protection film with excellent long-term corrosion resistance on magnesium alloy. Here, using an alkali-thermal process, we developed a $Mg(OH)_2/SiO_2$ composite film with long-term corrosion resistance on AZ91D magnesium alloy. The prepared sample's maximum capacitance semicircle had a diameter of around $4.0 \times 10^8 \ \Omega \ cm^2$, which was about 6 orders of magnitude higher than that of a Mg substrate. Having been immersed in 5 wt% NaCl solution for 168 h, the sample still kept its integrality, with only slight pitting marks left on the surface. The preparation process is straightforward and ecologically friendly, requiring no pretreatment samples and complicated experimental instruments, resulting in cost savings and increased efficiency.

1 Introduction

As an ideal engineering material [1, 2], magnesium alloy has excellent properties such as low density, high specific strength, and strong ductility. Similarly, magnesium also stays abundant in the crust. But compared with other alloys, the developments and research of magnesium alloys still fail to assess the effectiveness of its profound application. One of the main factors points to the active chemical properties of magnesium, which leads to the poor corrosion resistance of the alloy [3, 4]. To improve the corrosion resistance of magnesium alloys, many methods have been researched in a wide range in recent years, including surface modification [5, 6] and chemical inhibition [7, 8]. Besides, surface modification captured much attention as an economical and effective method. Due to the unique surface activity, magnesium alloy surfaces become exceedingly hard to electroplate [9]. And electroless plating often fails to play its role because of the poor adhesion of coating [10, 11]. Pretreatment is necessary for the surface of magnesium substrate [12, 13], but the high energy consumption and heavy cost in the pretreatment process [14, 15], as well as the use of a large number of harmful

substances [16], have gradually failed to meet the needs of current social development. Hence, it is urgent to find an economical, efficient, and environmentally-friendly method to prepare magnesium alloy corrosion-resistant coating [17].

Similar to magnesium alloy, aluminum alloy features a high chemical activity. Nevertheless, $Al_2O_3/Al(OH)_3$ composite membrane will be formed spontaneously by aluminum alloy in the atmosphere [18]. Not only does $Al_2O_3/Al(OH)_3$ composite film provide excellent corrosion protection for the substrate, but the formation process is also exceedingly simple and environmentally friendly. Hence, inspired by the characteristics above, researchers try to prepare spontaneous film with promising corrosion resistance on the magnesium alloy surface. However, being differentiated from aluminum alloy, the spontaneous $Mg(OH)_2/MgO$ composite film on the magnesium alloy surface features loose and porous, which can't provide corrosion protection for the substrate [19]. Thus, how to improve the compactness of $Mg(OH)_2$ film has developed into an urgent problem. Utilizing the alkaline hydrothermal method, Xu et al. [20] prepared a compact composite film of $Mg(OH)_2$ and MgO on the surface of magnesium alloy. Correspondingly, they adjusted the surface morphology by different temperatures and time treatments. As a result, the lowest corrosion current density of the sample occupied $1.083 \times 10^{-5} \ A \ cm^{-2}$, reaching about 1 order of magnitude lower than that of the substrate, and the corrosion protection effect was limited. To

✉ Jiyuan Zhu
zhujiyuanscut@163.com

1 College of Mechanical and Control Engineering, Guilin University of Technology, Guilin 541004, China

improve the corrosion resistance of $Mg(OH)_2$ film, Lin et al. [21] prepared β-TCMP/$Mg(OH)_2$ composite film on AZ31 magnesium alloy surface by one-step hydrothermal method. The corrosion current density of the sample decreased by about 3 orders of magnitude at most, and the impedance increased by about 3 orders of magnitude. However, during the experiment, after immersing in SBF solution for a long time (168 h), the sample was seriously corroded by the corrosive medium, and the magnesium alloy had almost dissolved. Research suggests that once the chloride concentration in the solution exceeds 30 mM, $Mg(OH)_2$ will begin to transform into soluble $MgCl_2$ [22] due to inherent instability, leading to the gradual disintegration of the film containing $Mg(OH)_2$, and then reducing the corrosion protection performance of the sample. Therefore, in the field of long-term effects, the $Mg(OH)_2$ film usually possess poor protection. Since then, the research on $Mg(OH)_2$ films has gradually mired in a bottleneck, with few breakthroughs.

Alkali heating treatment of magnesium alloys introduced numerous hydroxyl groups and generated $Mg(OH)_2$ on the surface [23, 24]. And most silicon compounds in water can be absorbed by $Mg(OH)_2$ particle surface [25]. Therefore, nano-SiO_2 powder was mixed into the reaction solution, and the $Mg(OH)_2$ composite film containing SiO_2 was prepared on the surface of AZ91D magnesium alloy by alkali-thermal method. As far as the author knows, there has been little research on the corrosion protection film of $Mg(OH)_2$ in recent years. In this method, the $Mg(OH)_2$/SiO_2 composite film was prepared on the surface of AZ91D magnesium alloy in one step without expensive drugs, complicated instruments, and pretreatment. The prepared sample was immersed in a 5 wt% NaCl solution for 168 h, and it remained intact with only slight pitting marks, which overcame the limitation that $Mg(OH)_2$ type coatings cannot provide long-term corrosion protection and offered a new idea and method for future research.

2 Materials and Methods

2.1 Materials

The material utilized in the experiment was AZ91D magnesium alloy (8.5%–9.5% Al, 0.45%–0.9% Zn, 0.17%–0.4% Mn) purchased by Hebei Tengshi Metal Materials Co., Ltd. (Xingtai, China). AZ91D magnesium alloy was cut into 22 mm×21 mm×4 mm specifications and a hole with a diameter of 3 mm punched on the surface. 8000 mesh nano-SiO_2 powder was purchased from Shanghai Yuanjiang Chemical Co., Ltd. (Shanghai, China). Absolute ethanol (C_2H_6O, AR) was purchased from Tianjin Fuyu Fine Chemical Co., Ltd. (Tianjin, China), and potassium hydroxide (KOH, AR) and calcium chloride ($CaCl_2$, 99.9%) were provided by Shanghai Yien Chemical Technology Co., Ltd. (Shanghai, China). Sodium chloride (NaCl) was supplied by China Shantou Xilong Technology Co., Ltd. (Guangdong, China). The high-temperature box furnace (KSL-1700X) utilized in the heating process was purchased from Hefei Kejing Material Technology Co., Ltd. (Anhui, China).

2.2 Methods

Polished with 800#, 1500#, and 2000# SiC sandpaper separately, AZ91D magnesium alloy sheets (15 mm×15 mm×3 mm) were ultrasonic cleaned in deionized water and absolute ethanol for 10 min to remove impurities on the surface and fat-soluble substances. Initially, adding 2.3 g 8000 mesh nano-SiO_2 powder and 2.68 g KOH solid into a beaker containing 23 ml deionized water, and stirring it uniformly by ultrasonic to obtain solution A. Equally, adding 2.67 g of $CaCl_2$ particles and 2.7 g KOH solids into another beaker containing 27 ml deionized water, and ultrasonically stirring to dissolve them to obtain solution B. After mixing and stirring the solutions A and B evenly, the mixture and the treated AZ91D magnesium alloy sheet were put into a crucible. Heated inside a muffle furnace for heating, the crucible was handled with a heating/holding temperature (205–235 °C) and a heating time (36–108 min), carrying out respectively in certain ranges, and the holding time set to 90 min; In order to form a contrast, only 50 ml of solution B was added to one group. The detailed data are listed in Table 1 below:

2.3 Sample Characterization

For visual observation, the Canon camera EOS M6 Mark II was used to image the sample surface before and after the immersion test. A scanning electron microscope (SEM, SU5000, Hitachi, Tokyo, Japan) was utilized to study the surface morphology of samples. The chemical composition of the samples surface was characterized by an energy-dispersive X-ray spectrometer (EDS, Bruker, Karlsruhe, Germany). X-ray photoelectron spectroscopy (XPS, Escalab, 250Xi, Thermo Scientific, Waltham, Massachusetts,

Table 1 Conditions required for preparing different samples

Sample	Heating time (min)	Heating/holding temperature (°C)	Remark
T36C220	36	220	
T73C220	73	220	
T108C220	108	220	
T73C205	73	205	
T73C235	73	235	
T73C220@B	73	220	50 ml solution B

America) with the Al Kα X-ray source (hv = 1486.6 eV) was utilized to measure the chemical composition and valence state of the samples. X-ray diffraction (XRD, SmartLab9, Rigaku, Tokyo, Japan) was used to study the phase structure of samples. According to the international standard test method ISO 2409-1992, the adhesion performance of the film on the sample surface was evaluated by a cross-cut tape test with a hundred-grid knife (QFH-A hundred-grid knife, Aipu Measuring Instrument Co., Ltd., Quzhou, China), the blade spacing is 1 mm ± 0.01 mm, and the test tape is 3 M Cat. 600 (Minnesota, USA). The surface morphology of the tested sample was photographed by video microscope (Video Microscope, G1200, Kailiwei, Guangdong, China).

2.4 Evaluation of Corrosion Performance

The corrosion resistance of the samples was evaluated by the CS2350H electrochemical workstation (Wuhan Corrtest Instrument Co., Ltd., Wuhan, China). A three-electrode system was utilized to test the performance of samples. A platinum plate worked as the auxiliary electrode, Ag/AgCl (saturated KCl) electrode played the part of the reference electrode, and 3.5 wt% NaCl aqueous solution posed as the electrolyte. Under the circumstances of room temperature, set the test sample as the working electrode, and the contact area with the electrolyte occupied 1 cm^2. Before the test, the sample was immersed in the solution for 30 min to ensure surface stability. The corrosion test was also performed with the untreated AZ91D magnesium alloy to form a contrast. To ensure the repeatability and accuracy of the experiment, corrosion tests were performed at least 3 times on all samples.

2.5 Immersion Test

To study the long-term corrosion resistance of the samples, carrying out a full immersion test. For the purpose of reproducibility, each sample was tested twice. Before the experiment, the sample was photographed and recorded as a weight of W_0. The surface area is S by measuring the size of the sample. After that, rinse the sample with deionized water, hang the sample in a beaker, add enough 5 wt% NaCl aqueous solution, and immerse the sample. The experiment was carried out at normal temperature and pressure, and samples were taken out every 24 h. For AZ91D samples, 200 g chromic anhydride and 1 L deionized water were used to prepare a clean solution to remove corrosion products on the surface, and then washed with deionized water and dried, which met ASTM G1-03 standard. For T73C220 sample, because the corrosion is light, there is basically no corrosion product attached to the surface, and chromate will affect the film layer. Therefore, only a large amount of deionized water is used to wash the sample. Record the weight of the

sample after each cleaning and air drying, and the corrosion weight loss resulted in $\Delta W = W_0 - W$, and the corrosion rate turned out $V = \Delta W/S$. Record the corrosion rate of AZ91D magnesium alloy as V_0, and the corrosion rate of the sample as V. To ensure the accuracy of the data, the samples were weighed five times to acquire the average value.

3 Results and Discussion

3.1 Sample Characterization

Figure 1 shows the images of samples prepared under different conditions. As shown in Fig. 1e, b, the overall morphology distribution of T108C220 and T73C205 samples is not uniform, and the two surfaces present nearly dark while existing black and gray patches. Among them, the size of black patches on the surface of T108C220 sample (Fig. 1e) is smaller, and gray color bands turn distributed around the black patches. In contrast, the T73C205 sample (Fig. 1b) has a smoother surface morphology and larger patch size. As shown in Fig. 1a, d, T36C220 sample and T73C235 sample also seem black. Although the surface morphology keeps relatively uniform, deeper black patches still exist distinctively. Differentiated from the first four samples, T73C220 sample (Fig. 1c) and T73C220@B sample (Fig. 1f) possess uniform surface morphology and inconspicuous distribution of color bands and patches, but the overall color of T73C220@B sample (Fig. 1f) tends to seem lighter. The experimental results show that the changes in heating time and heating/holding temperature will crucially affect the macroscopic surface morphology of the sample. Excessively high or low heating time and heating/holding temperature tend to induce color patches on the surface. Under the same conditions, when the heating time reaches 73 min and the heating/holding temperature reaches 220 °C, preparing T73C220 can reap more consistent surface morphology and uniform distribution.

Figure 2 illustrates SEM images of samples prepared under different conditions. The T108C220 sample (Fig. 2e) and T73C205 sample (Fig. 2b) show the surface conditions as previously speculated. Observed by the electron microscope image, the film on two surfaces seemed bumpy, and the granular protrusions distributed randomly, revealing more obviously under high-power electron microscope images. Similarly, distributed with a large number of folds facing the same direction, T108C220 and T73C205 possess massive cracks around their folds. As observed from the electron microscope images of T36C220 sample (Fig. 2a) and T73C235 sample (Fig. 2d), the film on two surfaces also seems slightly undulating. But there exists a slight distinction between the two samples. The T36C220 sample (Fig. 2a) appears uneven due to numerous granular microstructures randomly distributed

Fig. 1 Sample images prepared under different conditions **a** T36C220, **b** T73C205, **c** T73C220, **d** T73C235, **e** T108C220, **f** T73C220@B
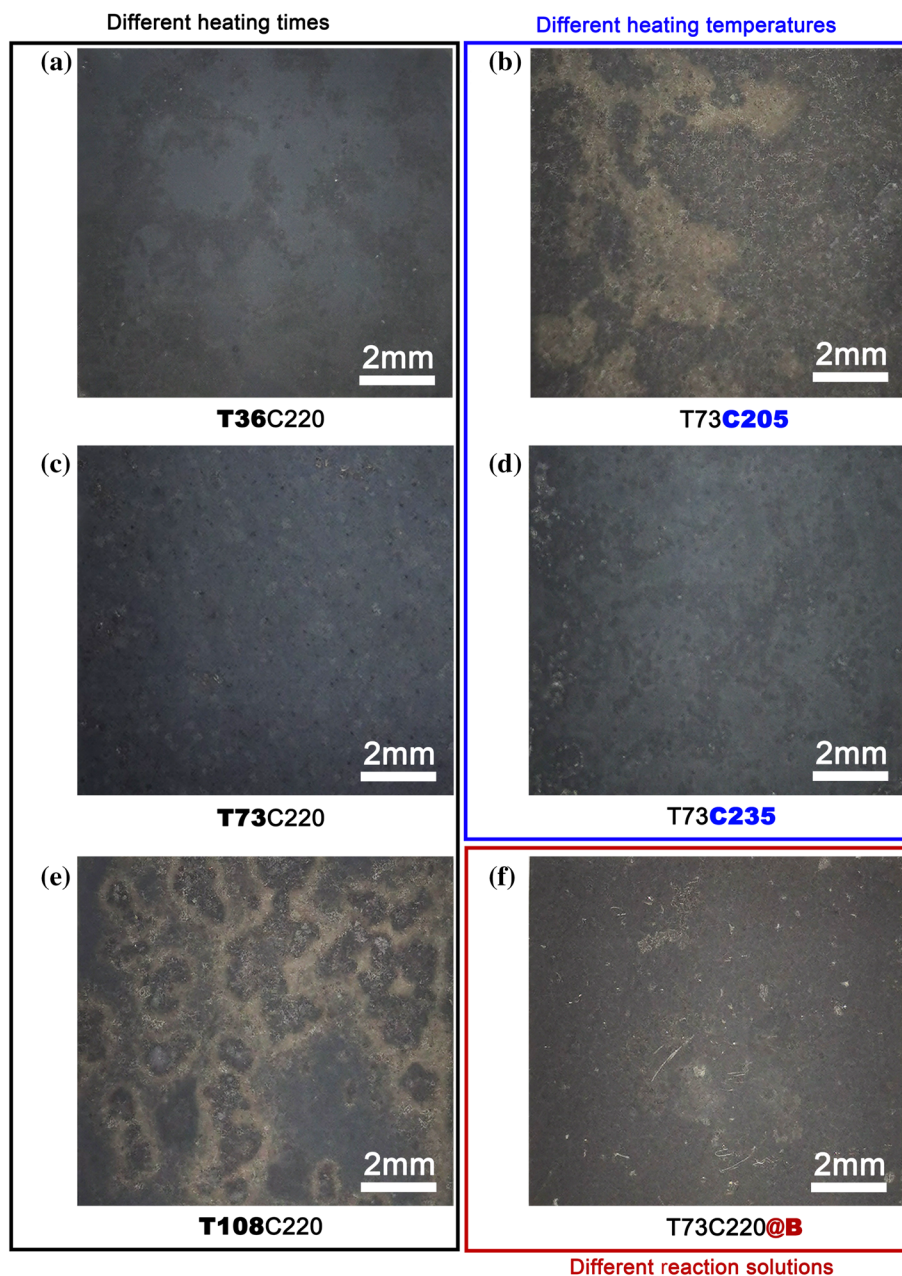
on the film. And T73C235 sample (Fig. 2d) stays in the same condition as T108C220 sample (Fig. 2e) and T73C205 sample (Fig. 2b). It is the fluctuation of the film that caused unevenness. Many wrinkles and cracks can be observed under high-power electron microscope images. The surface morphology of T73C220@B sample tends to show evenness on the macro-level (Fig. 1f), while the wrinkles and cracks on the surface of T73C220@B (Fig. 2f) sample stays voluminous densely distributed. But the T73C220 sample (Fig. 2c) is the flattest by contrast to the low-power electron microscope image, in which wrinkles possess slight fluctuation and uniform distribution. The high-power electron microscope image also shows that although cracks still exist on the film surface, the

cracks remain the least in terms of number and size among all samples. The experimental results elaborate that the morphology of the film on the surface of T73C220 sample features more uniform, flat, and consistent, both macroscopically and microscopically. Meanwhile, fewer wrinkles and cracks on the surface also mean that the film may have better corrosion protection under the same conditions [26].

3.2 Surface Composition Analysis

The films in this section were prepared under the conditions of heating time of 73 min, heating/holding temperature of 220 °C, and the reaction solution was AB mixture.
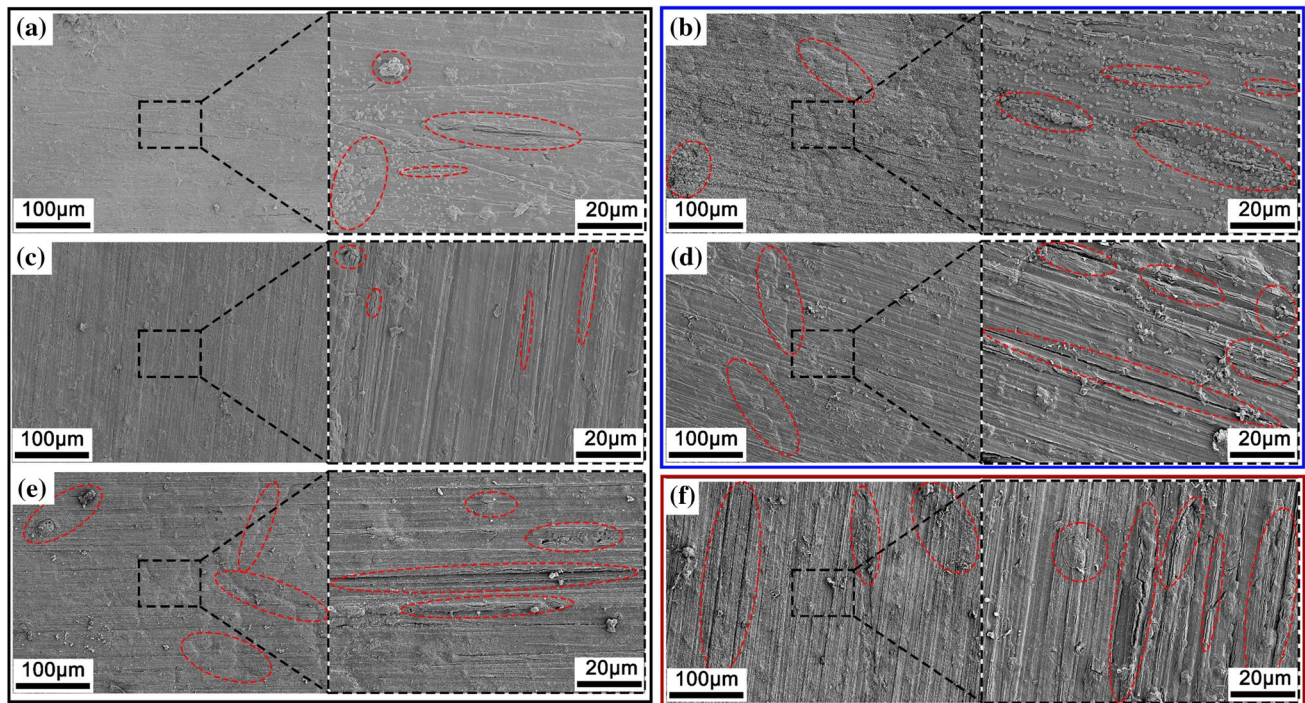
Fig. 2 SEM of samples **a** T36C220, **b** T73C205, **c** T73C220, **d** T73C235, **e** T108C220, **f** T73C220@B

Figure 3 shows the X-ray diffraction pattern of AZ91D, T73C220@B and T73C220 samples. The AZ91D, T73C220@B and T73C220 samples expatiated characteristic peaks at 32.4°, 34.6°, 36.9°, 48.1°, 57.8°, 63.5°, 69.1°, and 70.5°, which were from (100), (002), (101), (102), (110), (103), (112) and (201) in $Mg_{0.97}Zn_{0.03}$ (PDF 065-4596). The AZ91D, T73C220@B and T73C220 samples also exposited characteristic peaks at 36.1°, 40.1°, 41.9°, 43.7°, and 64.9°, depending on (411), (332), (422), (510), and (721) in $Al_{12}Mg_{17}$ (PDF 073-1148). The results flesh out that partial penetration of X-ray makes AZ91D magnesium alloy substrate of T73C220@B and T73C220 sample appear [27]. Differentiated from AZ91D magnesium substrate, the characteristic peaks of T73C220@B and T73C220 samples at 18.5°, 38.0°, 58.7°, and 62.1° were determined by (001), (101), (110) and (111) in $Mg(OH)_2$ (PDF 044-1482). The height and intensity of each diffraction peak stayed low, and the peak area appeared wide, which indicated that the crystal grain of $Mg(OH)_2$ contained in the film became small. In addition, T73C220 sample also showed characteristic peaks at 21.9°, 27.8°, 38.5°, 41.0°, 44.7° and 63.2° attributed to (100), (101), (110), (012), (200) and (121) of SiO_2 (PDF 083-0541). Similarly, the peak shape of this material looked inconspicuous, and the peak value stayed low, laying out that the SiO_2 material maintains a low load in the film and a scattered distribution. The XRD results show that the diffraction peaks indexed by $Mg(OH)_2$ can be clearly detected in both T73C220@B and T73C220 samples, which confirms the formation of $Mg(OH)_2$ in the films of the two samples. In addition, the diffraction peak indexed by SiO_2 was detected in T73C220 sample, which confirms the distribution of SiO_2 in T73C220 sample film.

Figure 4 illustrates the elemental composition of the film on the surface of the T73C220 sample analyzed by EDS (Energy Dispersive Spectrometer). Figure 4a shows each element's relative content in the sample, Fig. 4b shows SEM morphology, and Fig. 4c–f shows the EDS element mapping image on the film surface. As shown in the figure, the chemical elements are distributed continuously and uniformly according to the film morphology with no distinct defects and cracks.

To further detect the chemical composition of the film and then determine its characteristics, XPS came first in terms of analyzing the sample. Figure 5a illustrates the XPS full scanning spectrum of T73C220 sample. There are mainly O, C, Si, Al, Mg, and other elements in the film. Figure 5b–f shows the narrow scanning spectra of O 1s, C 1s, Si 2p, Al 2p, and Mg 1s.

Figure 5b illustrates the narrow scanning spectrum of characteristic element O 1 s. The O 1 s peak could be divided into two characteristic peaks. The first peak remained as a carbon–oxygen double bond (C=O) with a characteristic binding energy of 532.3 eV, which mainly existed in the chemical state of silica; and the other peak at ~531 eV was attributed to a carbon–oxygen single bond (C–O) and hydroxyl group (–OH). The C 1 s peak could be divided

Fig. 3 XRD diffraction pattern of AZ91D and T73C220 samples
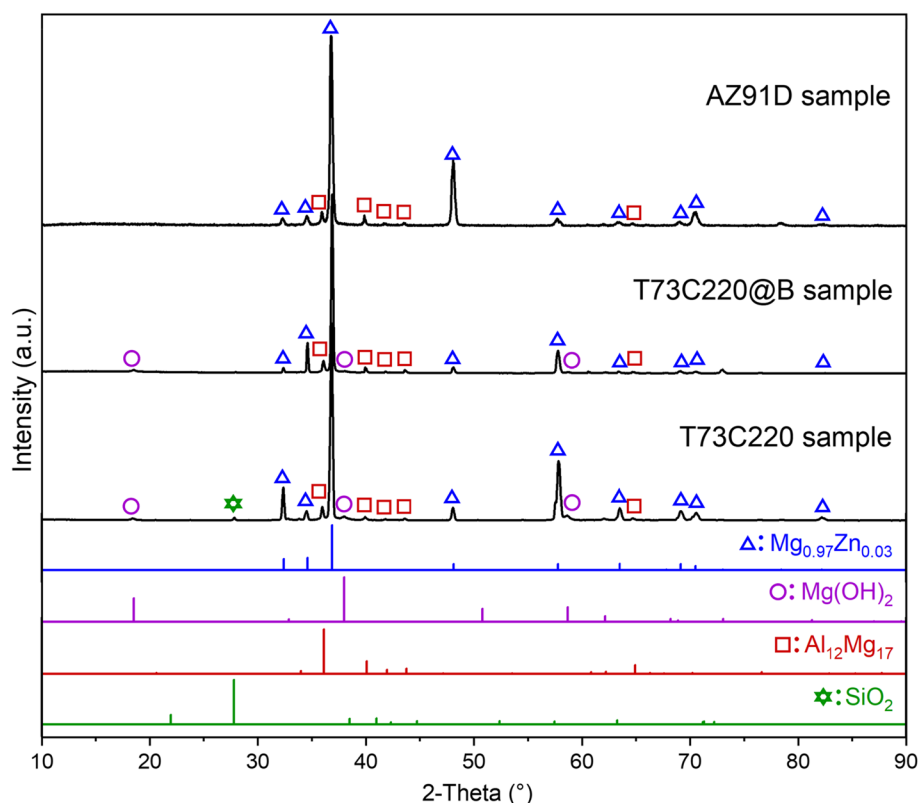
into three characteristic peaks (Fig. 5c). The first peak lay in carbon–carbon single bond (C–C) with a characteristic binding energy of 284.8 eV. The second peak was related to carbon–oxygen single bond (C–O) under ~286 eV, while the third peak at ~288.5 eV was attributed to the carbon–oxygen double bond (C=O). Figure 5d shows the narrow scanning spectrum of characteristic element Si 2p, and its characteristic binding energy lay at ~102.3 eV, which mainly stayed in the chemical state of silica. Figure 5e shows the narrow scanning spectrum of characteristic element Al 2p, and its characteristic binding energy lay at ~74 eV, which mainly stayed at the oxidation state signal of Al. Figure 5f shows the narrow scanning spectrum of characteristic element Mg 1 s with two characteristic peaks. Located at 1302.7 eV, the sample staying at the first peak existed as a magnesium element. The second peak pointed at 1304.3 eV, which meant the oxidation signal of Mg. Analyzed conjointly by XRD and XPS, the experimental results show the main components of the film on the surface of T73C220 sample are $Mg(OH)_2$ and SiO_2.

3.3 Adhesion Performance

Adhesion strength is a basic requirement for corrosion protection and a key factor for film durability, while excellent adhesion properties contribute to the long-term stability of the sample. Therefore, in order to characterize the adhesion

performance of the sample surface film, an adhesion cross-cut tape test was carried out [28]. Figure 6a shows the flow of the cross-cut tape test. The tape was applied to the surface of the cross-cut sample, and after ensuring that the tape adhered tightly to the sample, the tape was then pulled back in reverse at an angle of 180° as far as possible. Figure 6b shows the results of T73C220 sample surface test. As shown in the figure, the scratched edge is basically smooth at the cut edge with no obvious shedding phenomenon. The adhesion performance of the film was evaluated according to ISO 2409-1992 standard with the highest grade of 5B. The results show that the film on the sample surface has good adhesion to the substrate.

3.4 Analysis of Surface Corrosion Resistance

To characterize the corrosion resistance of samples, Fig. 7a–c gives the Nyquist plot, bode plot of |Z| versus frequency, and bode plot of phase angle versus frequency of different samples and AZ91D magnesium alloy in 3.5 wt% NaCl aqueous solution. The fitting data are connected by curves, and scattered points are experimental data. In the Nyquist plot (Fig. 7a), the capacitance semicircle diameter is related to the charge transfer resistance, which means a sample with better corrosion resistance usually has a larger capacitance semicircle diameter [29]. The capacitance semicircle diameter of AZ91D magnesium
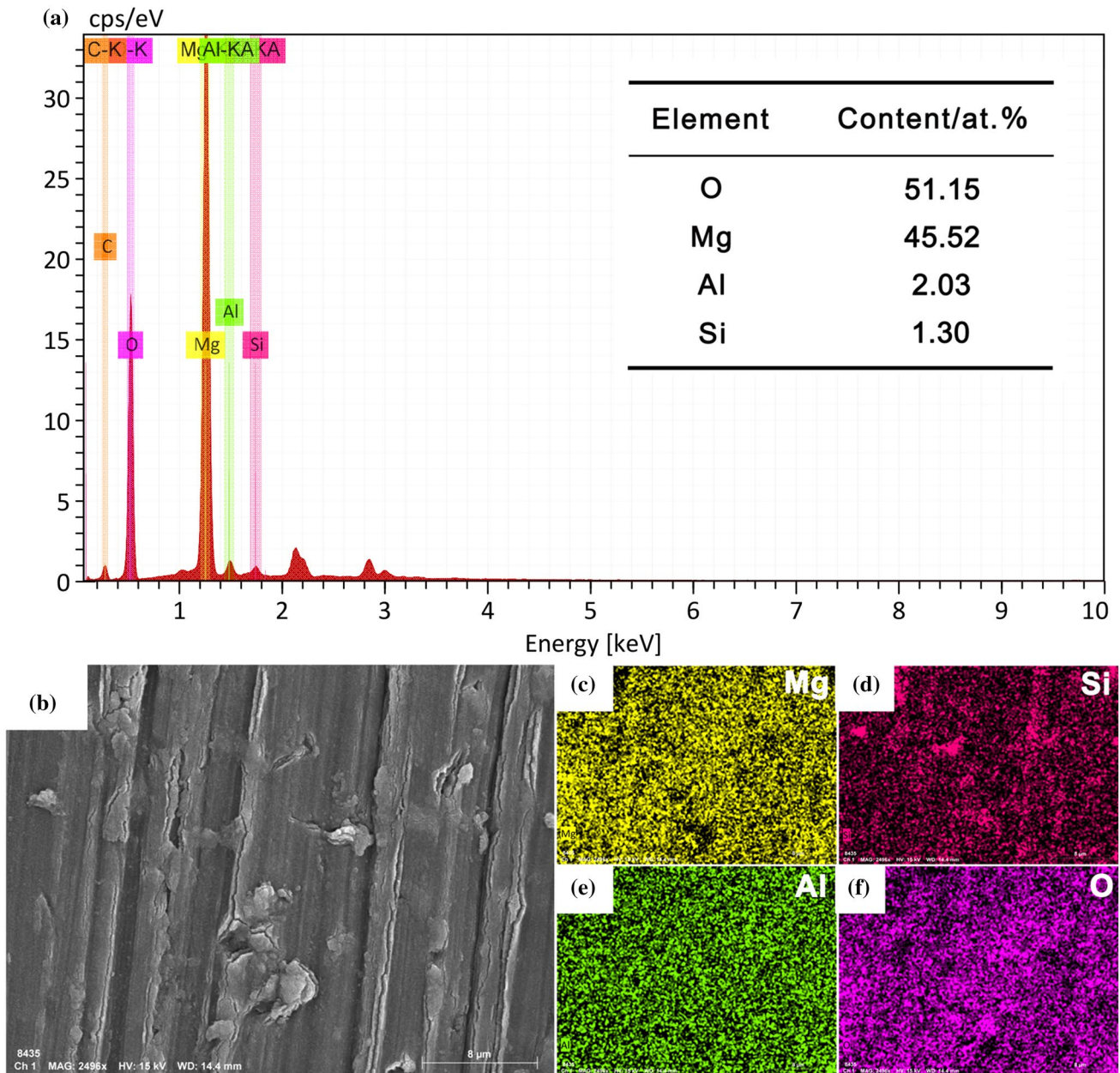
Fig. 4 On the surface of T73C220 sample **a** EDS analysis results; **b** SEM morphology and **c–f** EDS element mapping image

alloy occupied about 250 Ω cm^2, compared with that of T73C220 sample, which occupied about 4×10^8 Ω cm^2, reaching about 6 orders of magnitude higher. The results indicate that the diameter of the capacitor semicircle of T73C220 sample appeared much higher than that of the magnesium alloy substrate, which means the sample has extraordinary corrosion resistance. The bode plot of |Z| versus frequency can also verify the above characteristics (Fig. 7b). Generally, a higher value of |Z| in the Bode plot meets better corrosion resistance [30]. The experimental data demonstrates that the |Z| values of all treated samples

are higher than that of AZ91D magnesium alloy substrate. And the |Z| value of T73C220 sample remained at the top, occupying about 10^9 Ω cm^2, reaching 6 orders of magnitude higher than that of magnesium alloy substrate. The high phase angle in the high-frequency domain manifests a good repulsion performance of the sample, and the high modulus in the low-frequency domain means enhanced corrosion resistance [31]. As shown in Fig. 7c, the phase angles of all treated samples were also higher than the value of magnesium alloy substrate, but the T73C220 sample appears a higher phase angle in both high frequency
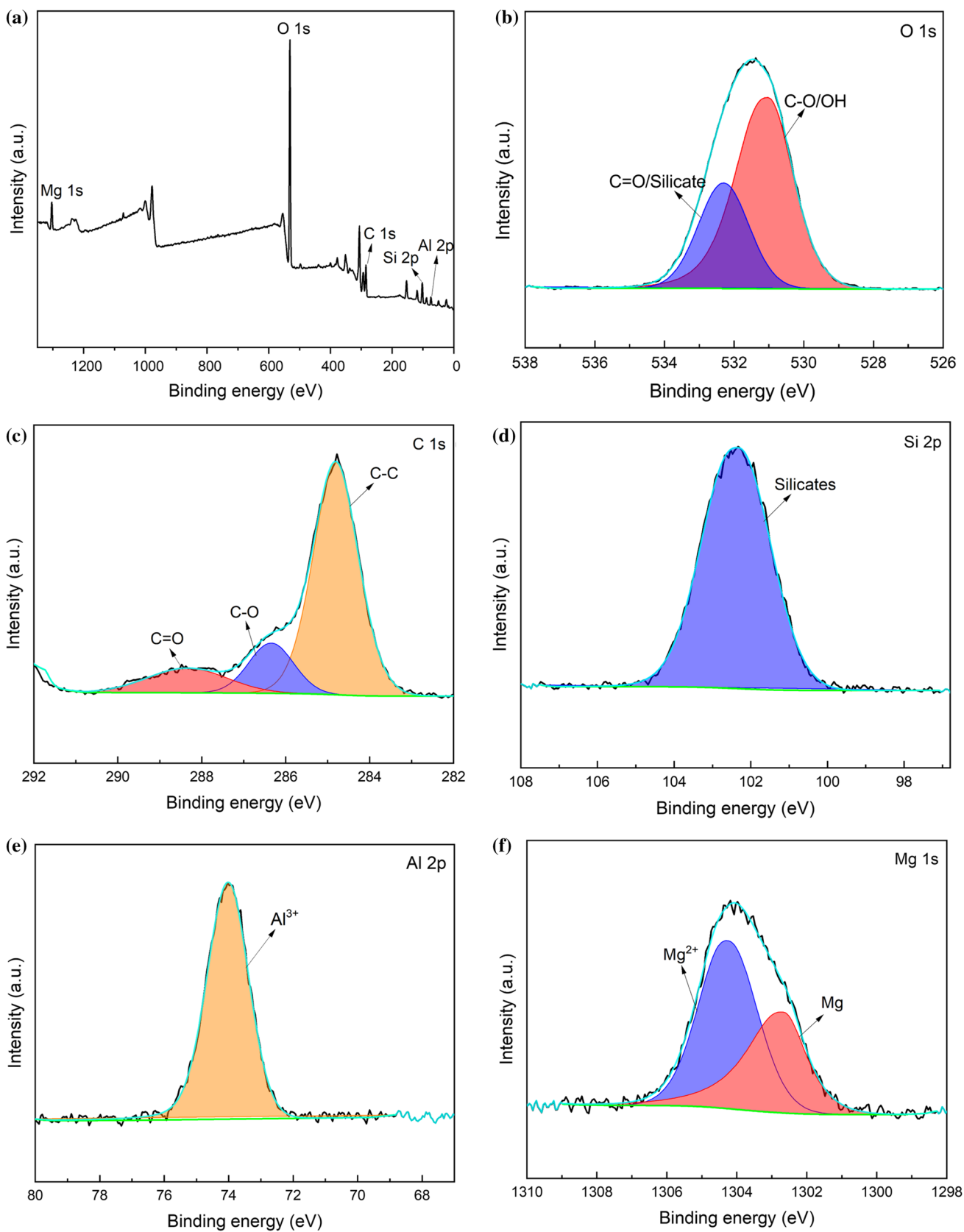
Fig. 5 T73C220 sample: **a** XPS full scanning spectrum; Narrow scanning spectrum, **b** O 1*s* region, **c** C 1*s* region **d**, Si 2*p* region, **e** Al 2*p* region, **f** Mg 1*s* region

Fig. 6 **a** The cross-cut tape test flow of the film and **b** the optical microscope image after the cross-cut tape test
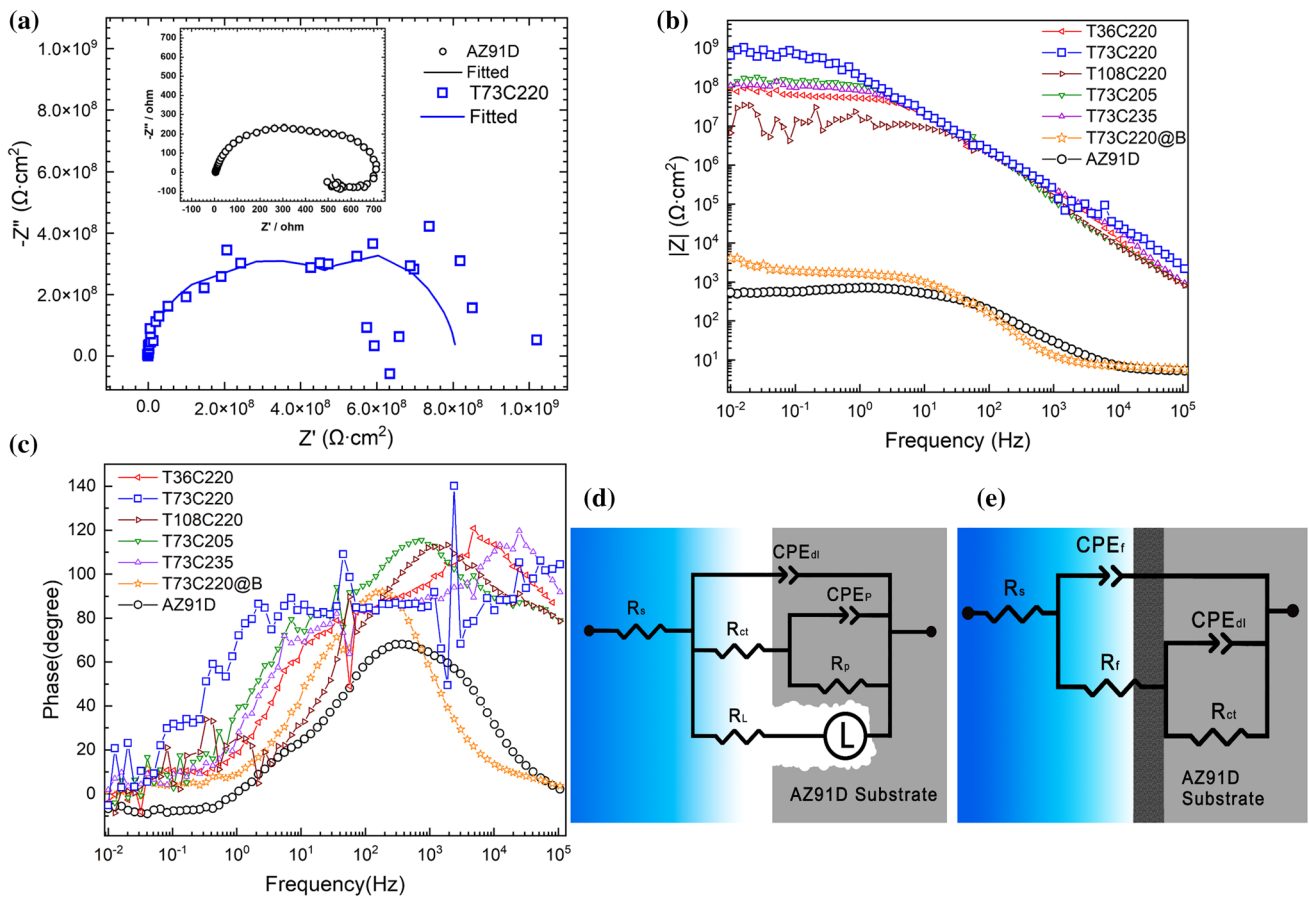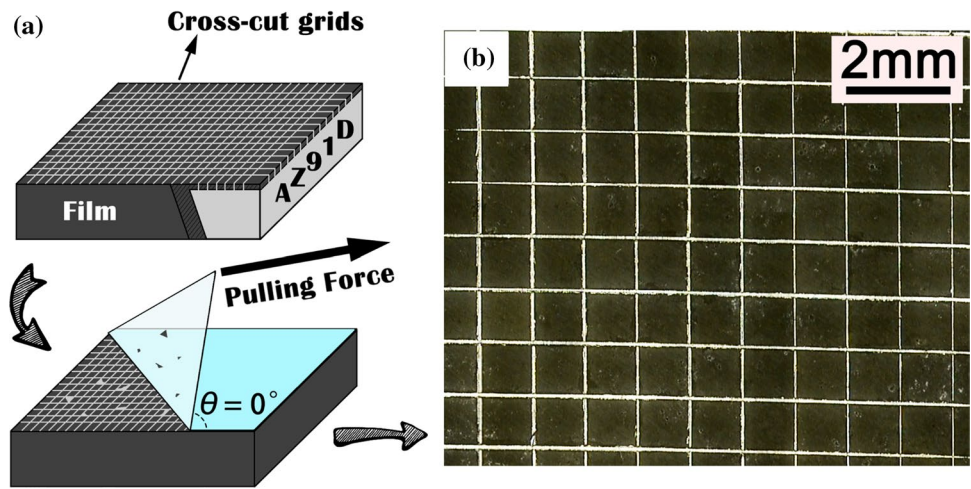

Fig. 7 Different samples in 3.5 wt% NaCl aqueous solution: **a** Nyquist plot, **b** bode plot of |Z| versus frequency, **c** bode plot of phase angle versus frequency, **d** the equivalent circuit model of AZ91D magnesium alloy, **e** the equivalent circuit model of T73C220 sample

and low frequency. Especially at low frequency, its phase angle value stayed much higher than other samples, showing a strong corrosion resistance and a preeminent repulsion performance. Among them, as shown in Fig. 7b, c, the corrosion resistance of T73C220@B sample is slightly improved compared with Mg substrate, but it is far less

than that of T73C220 sample prepared by different reaction solutions under the same treatment conditions. The main reason is that the main component of T73C220@B sample surface film is $Mg(OH)_2$. The properties of $Mg(OH)_2$ are unstable, and once the chloride concentration in the solution exceeds 30 mmol dm^{-3}, $Mg(OH)_2$

begins to transform into soluble $MgCl_2$ [32]. The reaction process is shown in Eq. (1).

$$Mg(OH)_2 + 2Cl^- \rightarrow MgCl_2 + 2OH^- \tag{1}$$
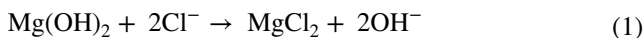
With the dissolution of $Mg(OH)_2$, the base metal is gradually exposed to the corrosive medium. Therefore, although the film on the surface of T73C220@B sample is uniform and flat in macroscopic (Fig. 1f) and microscopic aspects (Fig. 2f), the pure $Mg(OH)_2$ film can't provide better corrosion protection performance. The experimental results indicate that the composite film on the surface of T73C220 sample owned a highlighted corrosion protection effect. When the heating time is 73 min, the heating/holding temperature is 220 °C and the reaction solution is AB mixture, the $Mg(OH)_2/SiO_2$ composite film prepared on AZ91D magnesium alloy has the best corrosion resistance.

Figure 7d, e shows the equivalent circuit model (ECs) of AZ91D magnesium alloy and T73C220 sample. In the circuit, symbol R_s worked equivalent to the solution resistance, symbol R_f worked equivalent to the film resistance, and symbol R_{ct} worked equivalent to the charge transfer resistance. Equally, replacing the pure capacitor with a constant phase element (CPE) existed as a non-ideal capacitor set for circuit fitting [33]. In the fitting circuit of AZ91D (Fig. 7d), the capacitor circuit composed of CPE_p and R_p is related to the intermediate products Mg^{2+} produced after the contact between the Mg substrate and the solution, and represents the constant phase element capacitance and the diffusion resistance of electrolyte through the Mg(OH)2 layers, respectively [28, 34]. L (inductance) and R_L (inductance resistance) are used to describe the low-frequency inductance loop, which is attributed to the formation of pitting pits [35]. The experimental data evinced the R_{ct} of AZ91D magnesium alloy substrate reached 572.5 Ω while T73C220 sample reached 8.2756×10^7 Ω, calculating about 5 orders of magnitude higher than that of magnesium alloy. The fitting results prove T73C220 sample has a marvelous corrosion protection performance. At the same time, the disappearance of the low-frequency induction circuit also shows that the treated T73C220 sample has higher pitting resistance (Fig. 7e). Table 2 shows the details of the fitting data.

3.5 Immersion Test

The inherent instability of $Mg(OH)_2$ hindered the corrosion resistance. Once the chloride concentration exceeded 30 mM, $Mg(OH)_2$ would be transformed into soluble $MgCl_2$ [22], resulting in the dissolution of $Mg(OH)_2$ film, which would reduce the corrosion protection performance of the sample. Accordingly, to explore the corrosion protection effect of samples during a long-term immersion,

Table 2 Equivalent circuit fitting results of the EIS data

Sample	Rs (Ω cm²)	R_f (Ω cm²)	CPE_{dl} (µF/cm$^{-2} \cdot$s$^{(\alpha-1)}$)	Rct (Ω cm²)
AZ91D	5.25	–	31.10	572.5
T73C220	47.51	7.015×10^8	0.13	8.2756×10^7

AZ91D magnesium alloy and T73C220 samples were immersed in 5 wt% NaCl solution (857 mM) for Immersion test. In order to avoid the change of corrosion resistance caused by the depletion of corrosion components or the accumulation of corrosion products, the volume of 5 wt% NaCl solution used is 800 ml, and the volume/area ratio of liquid to sample is greater than 40 ml/cm². Each experiment was conducted twice to prove the measurements demonstrated reproducibility. Figure 8a illustrates the basic process of the experiment. First, weigh the sample before the immersion test. Secondly, take off the samples for washing and drying every 24 h during the experiment and weigh the samples again. Typically, to ensure the accuracy of the measurement results and to diminish the influence made by errors, weigh the samples five times each step, take the average value, record the data, and draw the result in Fig. 8b. As Table 3 suggested, in the immersion test of AZ91D magnesium alloy, with time accumulating, the ratio between weight loss and the area of the sample increased with time, and finally reached -80.500 mg/cm² after 168 h. In contrast, the change of the ratio between the weight loss and the area of T73C220 sample is almost negligible. After 168 h, the two groups of data reached 3.044×10^4 mg/cm² and 3.804×10^4 mg/cm², respectively. There is little difference between the two groups of data, and the change trend is consistent. The corrosion inhibition efficiency (η) of the film calculated by formula (2) is also given [36].

$$\eta = \frac{v_0 - v}{v_0} \times 100\% \tag{2}$$

In this equation, the symbol V_0 works equivalent to the corrosion rate of AZ91D magnesium alloy, and the symbol V works equivalent to the corrosion rate of the sample. As calculated by the equation, the corrosion inhibition efficiency of T73C220 sample reaches as high as 99.9996%.

Figures 9 and 10 demonstrate the surface change images of AZ91D magnesium alloy and T73C220 sample in the immersion test. Bubbles formed on the surface of the AZ91D sample continuously after the immersion of 5 wt% NaCl solution. After 24 h of immersion (Fig. 9b), the holes left by pitting corrosion appeared on the sample surface. Meanwhile, no obvious change in other positions
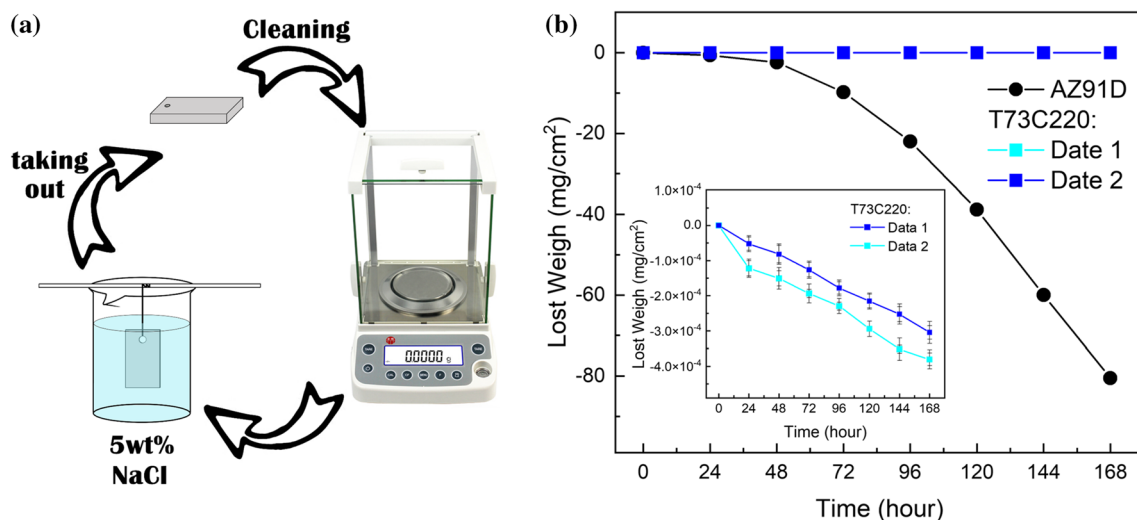
Fig. 8 **a** Schematic diagram of immersion test flow; **b** Immersion test data of AZ91D magnesium alloy and T73C220 sample in 5 wt% NaCl solution (The T72C220 sample showed two repeated measurements to prove reproducibility)

Table 3 Data obtained from the sample immersion test

Time (h)	AZ91D lost weigh (mg/cm^2)	T73C220 lost weigh (mg/cm^2)	
24	− 0.639	− 5.197 × 10^{-5}	− 1.220 × 10^{-4}
48	− 2.388	− 8.166 × 10^{-5}	− 1.507 × 10^{-4}
72	− 9.813	− 1.262 × 10^{-4}	− 1.938 × 10^{-4}
96	− 22.010	− 1.782 × 10^{-4}	− 2.297 × 10^{-4}
120	− 38.805	− 2.153 × 10^{-4}	− 2.942 × 10^{-4}
144	− 59.997	− 2.524 × 10^{-4}	− 3.517 × 10^{-4}
168	− 80.500	− 3.044 × 10^{-4}	− 3.804 × 10^{-4}

on the sample surface existed. After 48 h of immersion (Fig. 9c), numerous pitting holes emerged from the surface of AZ91D sample with a distinct increase in size, and the distribution was interconnected. After 72 h of immersion (Fig. 9d), this surface was covered by pitting holes. Hence, the number and size of pitting holes on the sample surface increased with time. After 168 h of immersion (Fig. 9h), its surface had become exceedingly loose, and any external force would make the surface produce metal fragments and fall off. The results demonstrate that AZ91D magnesium alloy has totally lost its fundamental function as a metal component after immersion for 168 h.

As shown in Fig. 10, when T73C220 sample was immersed in 5 wt% NaCl solution for a short time, there existed inconspicuous changes and bubbles on the surface of the sample. After 24 h of immersion (Fig. 10b), scattered white spots appeared on the surface, which was generated by pitting. After 168 h of immersion (Fig. 10h), the pitting holes on the surface of T73C220 sample became slightly apparent, and the number and size of pitting holes did not

change manifestly with the increase of time. The results indicate that T73C220 sample has a promising corrosion resistance in the immersion experiment, and the pitting might be related to the wrinkles and tiny cracks observed under the electron microscope (Fig. 2e, f).

The experimental results demonstrate that when the heating time is 73 min, the heating/holding temperature is 220 °C, and the reaction solution is AB mixed solution, the treated $Mg(OH)_2/SiO_2$ composite film tends to possess the optimum corrosion resistance. After being immersed in 5 wt% NaCl solution (857 mM) for a long time (168 h), the surface film does not gradually dissolve as time increases, which manifests an excellent long-term corrosion resistance of the samples.

Figure 11a–c shows the detailed corrosion morphology of T73C220 sample after immersing for 24 h, 96 h and 168 h, respectively. After 24 h immersion, there existed no obvious corrosion trace on a macro level (Fig. 10b). However, as shown in Fig. 11a, there were more obvious concave areas on the surface with slightly different shapes, and the concave depths were shallow with no obvious corrosion products attached around depressions. After the sample was immersed for 96 h (Fig. 11b), it can be observed that the size and depth of the recessed area increased obviously, and numerous corrosion products were distributed around the depressions. After the sample was immersed for 168 h (Fig. 11c), no further dimensional changes were observed in the depressed area, but a large number of bulges formed by corrosion products surrounded and gradually covered the depressed area. Furthermore, the morphology of the film around the depression was still intact, and no obvious cracking or shedding phenomenon was observed, which indicated that the coating was continuously protected. At the same
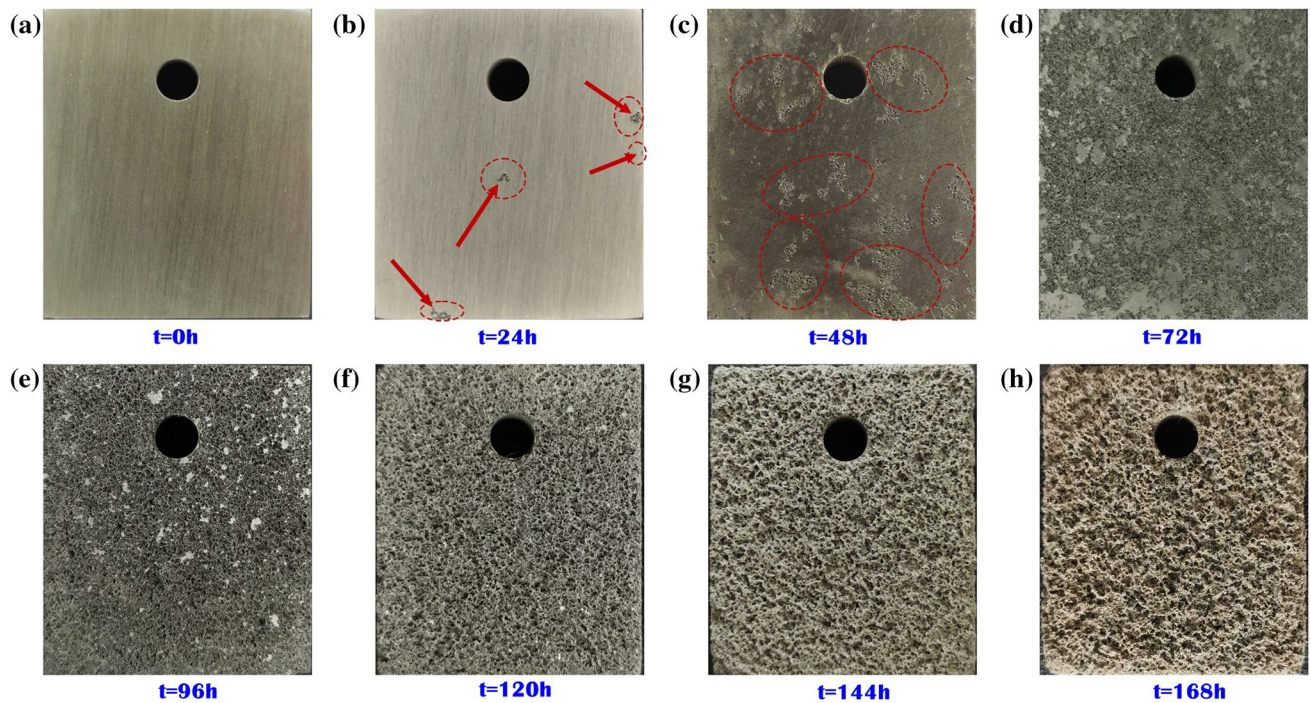
Fig. 9 The immersion test images of AZ91D sample in 5 wt% NaCl solution, **a** 0 h, **b** 24 h, **c** 48 h, **d** 72 h, **e** 96 h, **f** 120 h, **g** 144 h, **h** 168 h
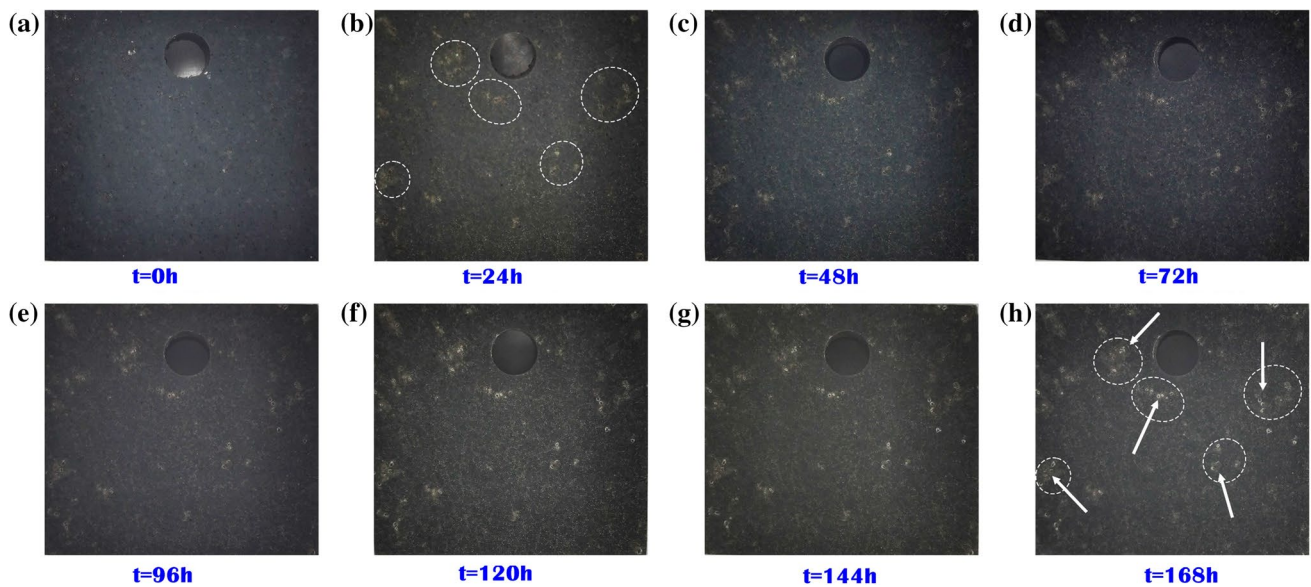

Fig. 10 The immersion test images of T73C220 sample in 5 wt% NaCl solution, **a** 0 h, **b** 24 h, **c** 48 h, **d** 72 h, **e** 96 h, **f** 120 h, **g** 144 h, **h** 168 h

time, the sample still showed local pitting after the sample was immersed in 5 wt% NaCl solution for 168 h, and the local corrosion area did not spread to the overall corrosion, which again proved the excellent corrosion protection performance of T73C220 sample.

Figure 11d–k shows the EDS scanning electron microscope morphology and spectrum results of the surface of

T73C220 sample after immersion test. As shown in the figure, the elements are widely and uniformly distributed on the surface of T73C220 sample according to the film morphology outside the concave area. Among them, Al element (Fig. 11g) and Si element (Fig. 11i) are mainly distributed in a surrounding way in the concave area, and show a scattered distribution inside the concave area with obvious
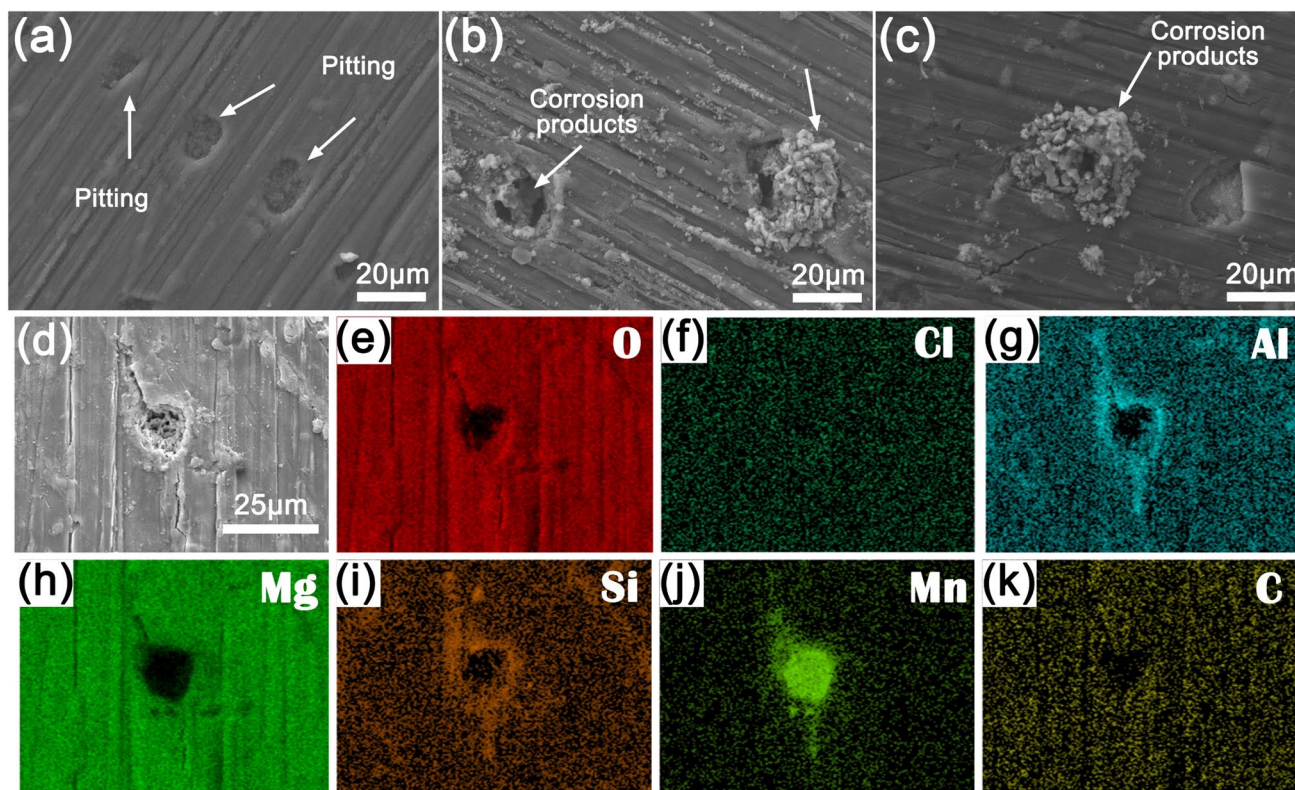
Fig. 11 After immersion test T73C220 sample in 5 wt% NaCl solution, the electron microscope image after **a** 24 h, **b** 96 h, **c** 168 h; **d** the EDS scanning electron microscope morphology, and **e–k** the mapping image of each element

element enrichment. In addition, the Mn element is obviously enriched in the depressed area (Fig. 11j). The enrichment of Al, Si and Mn is mainly related to the formation of corrosion products. The generation and aggregation of a large number of corrosion products gradually cover the holes generated by corrosion, and the size of the holes gradually decreases. The solution containing a corrosive medium cannot attack the Mg alloy substrate through the corrosion holes, and the protective effect of the corrosion product layer is further enhanced, thus inhibiting the corrosion of AZ91D magnesium alloy in NaCl solution [37].

4 Conclusions

In this paper, $Mg(OH)_2/SiO_2$ composite film with excellent corrosion resistance was prepared by a one-step reaction on the surface of AZ91D magnesium alloy by alkali-thermal method without pretreatment. The diameter of the capacitor semicircle in the Nyquist plot of the sample occupied 4.0×10^8 Ω cm^2, which reached 6 orders of magnitude higher than that of magnesium alloy substrate, showing excellent corrosion protection performance. The immersion test results also indicate that $Mg(OH)_2/SiO_2$ composite film can provide excellent long-term corrosion resistance,

breaking with the convention that the corrosion resistance of films containing $Mg(OH)_2$ stays usually poor. Likewise, this method avoids the disadvantages of high cost and high energy consumption of magnesium alloy pretreatment, providing a new method for improving the corrosion protection performance of magnesium alloy.

Declarations

Conflict of interest The authors declare that they have no conflict of interest.

References

1. Y. Yang, X. Xiong, J. Chen, X. Peng, D. Chen, F. Pan, J. Magnes. Alloy. **9**, 705 (2021)
2. P. Predko, D. Rajnovic, M.L. Grilli, B.O. Postolnyi, V. Zemcenkovs, G. Rijkuris, E. Pole, M. Lisnanskis, Metals **11**, 1133 (2021)
3. H. Liu, F. Cao, G.-L. Song, D. Zheng, Z. Shi, M.S. Dargusch, A. Atrens, J. Mater. Sci. Technol. **35**, 2003 (2019)
4. F. Peng, D.D. Zhang, X.Y. Liu, Y. Zhang, J. Magnes. Alloy. **9**, 1471 (2021)

5. P.C. Banerjee, S. Al-Saadi, L. Choudhary, S.E. Harandi, R. Singh, Materials 12, 136 (2019)

6. G. Yang, H. Yang, L. Shi, T. Wang, W. Zhou, T. Zhou, W. Han, Z. Zhang, W. Lu, J. Hu, ACS Biomater. Sci. Eng. 4, 4289 (2018)

7. N.A. Johari, J. Alias, A. Zanurin, N.S. Mohamed, N.A. Alang, M.Z.M. Zain, J. Coat. Technol. Res. 19, 757 (2022)

8. S.Y. Wang, Q. Li, X.K. Zhong, L.Q. Li, F.N. Chen, F. Luo, Y. Dai, H. Gao, F. Liu, H.X. Zhang, T. I. Met. Finish. 90, 78 (2012)

9. L.P. Wu, J.J. Zhao, Y.P. Xie, Z.D. Yang, T. Nonferr. Metal. Soc. 20, S630–S637 (2010)

10. C. Zhang, B. Liu, B. Yu, X. Lu, Y. Wei, T. Zhang, J.M.C. Mol, F. Wang, Surf. Coat. Tech. 359, 414 (2019)

11. H. Zhao, S. Cai, S. Niu, R. Zhang, X. Wu, G. Xu, Z. Ding, Ceram. Int. 41, 4590 (2015)

12. J.Y. Hu, Q. Li, X.K. Zhong, L. Zhang, B. Chen, Prog. Org. Coat. 66, 199 (2009)

13. L. Guo, C. Gu, J. Feng, Y. Guo, Y. Jin, J. Tu, J. Mater. Sci. Technol. 37, 9 (2020)

14. T. Lkhagvaa, Z.U. Rehman, D. Choi, J. Coat. Technol. Res. 18, 1 (2021)

15. J. Zhang, C.Y. Wu, Prog. Org. Coat. 66, 387 (2009)

16. D. Seifzadeh, H.K. Mohsenabadi, Bull. Mat. Sci. 40, 407 (2017)

17. A.A. Olajire, J. Mol. Liq. 269, 572 (2018)

18. T. Dursun, C. Soutis, Mater. Des. 56, 862 (2014)

19. J.H. Nordlien, K. Nisancioglu, S. Ono, N. Masuko, J. Electrochem. Soc. 143, 2564 (1996)

20. R. Xu, Y. Shen, J. Zheng, Q. Wen, Z. Li, X. Yang, P.K. Chu, Surf. Coat. Tech. 309, 490 (2017)

21. Y. Lin, S. Cai, S. Jiang, D. Xie, R. Ling, J. Sun, J. Wei, K. Shen, G. Xu, J. Mech. Behav. Biomed. Mater. 90, 547 (2019)

22. D.D. Zhang, F. Peng, X.Y. Liu, J. Alloy. Compd. 853, 157010 (2021)

23. C. Pan, Y. Hu, Y. Hou, T. Liu, Y. Lin, W. Ye, Y. Hou, T. Gong, Mater. Sci. Eng. C 70, 438 (2017)

24. L.C. Li, J.C. Gao, Y. Wang, Surf. Coat. Tech. 185, 92 (2004)

25. D.B. Kent, M. Kastner, Geochim. Cosmochim. Acta. 49, 1123 (1985)

26. Y.N. Xue, X. Pang, B.L. Jiang, H. Jahed, Mater. Corros. 70, 268 (2019)

27. Q. Luo, Q.Z. Cai, Z.T. Fan, Z. Zhao, Int. J. Cast. Metals Res. 25, 341 (2012)

28. C.-L. Ko, Y.-L. Kuo, S.-H. Chen, S.-Y. Chen, J.-Y. Guo, Y.-J. Wang, Thin Solid Films 709, 138151 (2020)

29. C. Das, E. Kastania, J. Witt, O. Ozcan, Mater. Corros. 73, 427 (2022)

30. Y. Wang, D. Yan, Y. Zhu, J. Liu, D. Song, L. Chen, T. Zhang, K. Cheng, M. Zhang, J. Wang, Mater. Corros. 70, 1222 (2019)

31. L.M. Calado, M.G. Taryba, M.J. Carmezim, M.F. Montemor, Corros. Sci. 142, 12 (2018)

32. L.W. Zhu, C. Peng, K. Kuroda, M. Okido, Mater. Res. Express 6, 116424 (2019)

33. Y.H. Chen, W.H. Yao, L. Wu, J. Chen, F.S. Pan, Coatings 11, 59 (2021)

34. M.Y. Chen, Y.Q. Chen, W.T. Zhang, S. Zhao, J. Wang, J.L. Mao, W. Li, Y.C. Zhao, N. Huang, G.J. Wan, RSC Adv. 6, 15247 (2016)

35. M.F. He, L. Liu, Y.T. Wu, Z.X. Tang, W.B. Hu, Corros. Sci. 50, 3267 (2008)

36. X. Lu, Y. Li, P. Ju, Y. Chen, J. Yang, K. Qian, T. Zhang, F. Wang, Corros. Sci. 148, 264 (2019)

37. P.X. Zhao, W. Wu, Z.Y. Ma, Y. Dan, Methods Mater. 69, 204 (2022)